Impact of Interactive Radiative Transfer on the Macroscopic Behavior of Cumulus Ensembles. Part II: Mechanisms for Cloud–Radiation Interactions

KUAN-MAN XU AND DAVID A. RANDALL

Department of Atmospheric Science, Colorado State University, Fort Collins, Colorado

(Manuscript received 26 October 1993, in final form 5 July 1994)

ABSTRACT

The two-dimensional UCLA cumulus ensemble model is used to examine the impact of cloud–radiation interactions on the macroscopic behavior of cumulus ensembles. Two sets of simulations are performed with noninteractive (NI) and fully interactive (FI) radiative transfer, and with prescribed large-scale advective effects. The time-varying horizontally averaged radiative heating rates Q_R from the FI simulations are used to prescribe the time-varying, horizontally homogeneous Q_R in the NI simulations. The effects of both longwave radiation and diurnally varying solar radiation are examined from these two sets of simulations.

The diurnally varying solar radiation can drive a diurnal cycle of deep convection over the tropical oceans by stabilizing the large-scale environment during the daytime relative to the nighttime. The results presented in this study confirm the dominant role of the direct radiation–convection interaction mechanism for the diurnal cycle of oceanic precipitation. Comparison of the results of the FI and NI simulations suggests that the horizontal differential heating mechanism of Gray and Jacobson plays a secondary role in the diurnal cycle of precipitation. The presence of interactive radiation in the FI simulation, however, postpones the maxima and minima of convective activity due to the greater persistence of upper-tropospheric clouds. These clouds can survive against the solar absorption effects during the daytime.

The impact of longwave–cloud interactions on the macroscopic behavior of cumulus ensembles is a slightly stronger modulation of cumulus activity by large-scale processes. Upper-tropospheric clouds are somewhat more active and last longer in the presence of interactive radiation. The longwave–cloud interactions are achieved by the so-called continuously destabilizing mechanism, which has its greatest effects on thin cloud layers.

1. Introduction

Hypothetical mechanisms for cloud–radiation interactions are based on the gradient and/or magnitude of radiative heating rates due to the presence of clouds. They include (i) horizontal differential heating between cloudy and clear regions, which produces a secondary circulation (Gray and Jacobson 1977); (ii) continuously destabilizing effects of anvil cloud layers, which enhance the convective circulations of the cloud layers (Webster and Stephens 1980; Chen and Cotton 1988; Dudhia 1989); and (iii) in-cloud radiative heating and radiative destabilization, generating buoyant turbulence in the anvil clouds and prolonging their life span (Lilly 1988). The Gray–Jacobson mechanism was originally intended to explain the observed diurnal cycle of oceanic precipitation as a result of the large day versus night differences in the radiative heating profiles between mesoscale cloudy regions and the surrounding clear regions. According to Gray and Jacobson (1977),

> The atmosphere surrounding organized cloud regions adjusts to its large radiational cooling at night through extra subsidence. This extra nighttime subsidence increases low-level convergence into the adjacent cloud regions. During the day solar heating reduces tropospheric radiation loss. Clear region subsidence warming and cloud region low-level convergence are substantially reduced.

The Gray–Jacobson mechanism can be characterized as a *radiation–dynamics–convection interaction*, which involves the diurnal variation of the large-scale or mesoscale vertical motion (Gray and Jacobson 1977). Other mechanisms for diurnal variation of oceanic precipitation (e.g., Randall et al. 1991) are (i) *direct radiation–convection interactions*, in which solar absorption in the upper portion of cloud masses is the main stabilizing effect favoring less convection during the daytime; (ii) remote influence of the continents; and (iii) diurnal variations of the sea surface temperature. Only two of these four mechanisms, that is, radiation–dynamics–convection interactions and direct radiation–convection interactions, will be examined in this study.

Since the emphasis of this study is on the impact of cloud–radiation interactions on the macroscopic behavior of cumulus ensembles, the large-scale processes

Corresponding author address: Dr. Kuan-Man Xu, Dept. of Atmospheric Science, Colorado State University, Fort Collins, CO 80523.

are prescribed; that is, feedback of the convective activity and radiation on the large-scale circulations is not allowed. A unique aspect of this study is the design of the explicit simulations of cumulus ensembles. Miller and Frank (1993) performed a similar pair of simulations using a mesoscale model with parameterized cumulus convection. In the current study, two simulations are performed, one with fully interactive radiative transfer and the other with horizontally uniform radiative heating rates determined from the domain-averaged heating rates of the fully interactive simulation. Thus, the domain-averaged radiative effects and their *time evolution* are identical in the two simulations. The horizontal differential heating between cloudy and clear regions is removed in the noninteractive simulation, but the domain-averaged radiative effects of clouds are still included. Some previous studies (e.g., Dudhia 1989; Tao et al. 1991, 1993), as mentioned in Xu and Randall (1995, hereafter Part I), compared a fully interactive simulation with a simulation with zero radiative heating rate. Another feature of the current study is that long (>10 days) integrations are performed, instead of runs of a few hours to a day as in previous studies. Thus, the statistical behavior of cumulus ensembles can be examined, instead of the temporal evolution of an individual case as in most previous studies (e.g., Dudhia 1989; Miller and Frank 1993).

Randall et al. (1991) simulated the diurnal cycle of oceanic precipitation using the CSU general circulation model (GCM). The explicit simulation of cumulus ensembles described in this paper can be a useful check on some important aspects of the GCM simulations. The main objective in Part II of this two-part study is to identify which cloud–radiation interaction mechanisms have a significant impact on the macroscopic behavior of cumulus ensembles and to identify the dominant mechanism for the diurnal variations of tropical oceanic precipitation.

The numerical simulations are briefly described in section 2. Results from cumulus ensemble model (CEM) simulations with fully interactive radiation and noninteractive radiation are presented in sections 3 and 4. Mechanisms for cloud–radiation interactions are examined in section 5. A summary and discussion are provided in section 6.

2. Numerical simulations

Two sets of idealized simulations of tropical convective systems (Table 1) were performed with (i) time-independent geostrophic wind components, (ii) interactive or noninteractive radiative transfer, and (iii) time-independent or time-varying large-scale advective effects, using the University of California at Los Angeles (UCLA) CEM with a radiation parameterization as described in Part I. The prescribed large-scale variables are horizontally uniform in the model. In all simulations, a height-independent, geostrophic x-component wind (5 m s^{-1}) is used. Ageostrophic wind shear can be produced in all integrations.

TABLE 1. A summary of the design of numerical simulations used in this study.

Simulation	Radiation		Large-scale advective effects
	Solar	Infrared	
I04	No	Interactive	Time varying
N04	No	Noninteractive	Time varying
I05	Interactive	Interactive	Time invariant
N05	Noninteractive	Noninteractive	Time invariant

In one set of simulations (I04 and N04; Table 1), we use time-varying large-scale advective effects similar to those used in simulations Q02 and Q03 of Xu et al. (1992) except that the magnitude is half as large. The period of the prescribed time variation is 27 h. This set of simulations includes only longwave radiative transfer. In another set of simulations (I05 and N05), both longwave and diurnally varying shortwave radiative transfer are included, but with time-independent large-scale advective effects. Therefore, there is only one externally imposed temporal period in each set of simulations. I04 and I05 are performed with interactive radiative transfer, and N04 and N05 with noninteractive radiation. The radiation module is called every 150 s using the "accumulated" method as described in Part I.

Each simulation was run for 15 days of physical time with a time step of 10 s. The remaining aspects of these simulations are identical to those of Q02 and Q03 in Xu et al. (1992) and the sensitivity tests in Part I. For example, the underlying surface is an ocean with a fixed sea surface temperature (299.9 K). The domain size is 512 km, with a horizontal grid size of 2 km. The sensitivity of results, especially those of the surface precipitation rate, the fractional cloudiness, and the shortwave and longwave heating rates, on the horizontal domain size and the horizontal resolution was examined in Part I. The overall impact due to the increase of the domain size or the horizontal resolution was very small.

3. Results: Impact of solar radiation

The impact of solar radiation on cumulus activity is examined from simulations I05 and N05. Both the Gray–Jacobson (1977) and direct radiation–convection interaction mechanisms for the diurnal cycle of oceanic cumulus convection are explored in detail. The pair of simulations described in this section includes diurnally varying solar radiation, infrared radiation, and time-independent large-scale advective effects.

Figure 1a shows the time sequence of the ensemble mean of the surface precipitation rate $\langle P \rangle$ for I05 and

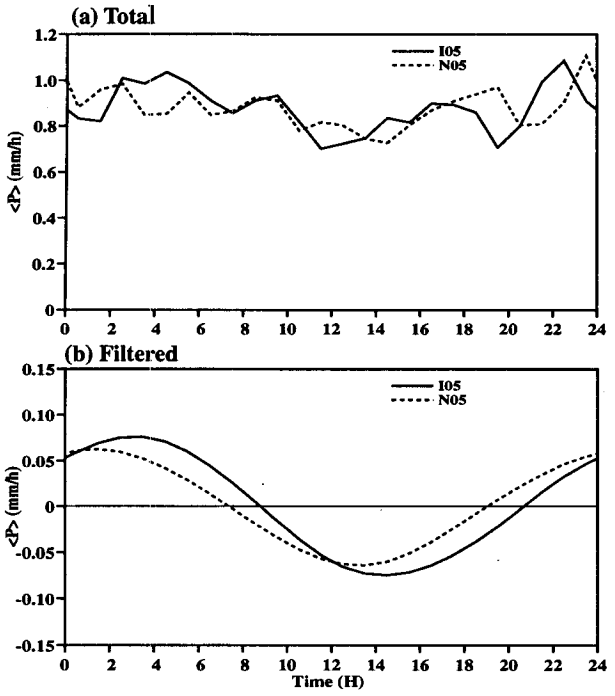

FIG. 1. Time sequence of the ensemble mean of (a) total surface precipitation rate, and (b) the filtered one for I05 (solid) and N05 (dashed). The abscissa is the local time.

N05. Here $\langle P \rangle$ is averaged over the entire domain (512 km) before the ensemble average is taken. The ensemble average is defined with respect to the phase of the diurnal cycle (local time) in I05 and N05. The time-sequence plots in this paper are, hereafter, for the ensemble means unless mentioned otherwise. Fluctuations around the ensemble mean are not examined. Xu et al. (1992) discussed the nonmodulated high-frequency fluctuations in detail.

Figure 1a indicates that $\langle P \rangle$ exhibits a diurnal variation in both simulations regardless of whether radiation is interactive or noninteractive. Convective activity is generally less intense during the daytime than during the nighttime in both simulations. This indicates that the direct radiation–convection interaction is the dominant mechanism for the diurnal cycle. This point will become more evident as more detailed results are presented later. Figure 1a also shows that some high-frequency fluctuations with a period of a few hours exist, however. Some fluctuations other than the semidiurnal mode would presumably be eliminated from the ensemble mean if the simulations were extended long enough. In the absence of large-scale advective effects, similar diurnal variations can occur (not shown).

In order to gain insight into the diurnal cycle of cumulus convection, a bandpass filter (Murakami 1979) is applied to eliminate any nondiurnal signal. This bandpass filter retains those signals with a period between 20 and 27 h. (The time-sequence plots presented in this section are, hereafter, for filtered variables unless mentioned otherwise.) Figure 1b shows the filtered $\langle P \rangle$. The amplitude of the diurnal variation in $\langle P \rangle$ (18% of the mean in Fig. 1a) is about 0.16 mm h^{-1} in I05, or 3.8 mm d^{-1}, which is a typical magnitude observed in the Tropics (Gray and Jacobson 1977) or simulated by the CSU GCM (Randall et al. 1991). The maximum $\langle P \rangle$ occurs in the early morning, and the minimum in the early afternoon. This is also consistent with some observations (e.g., Gray and Jacobson 1977; Hendon and Woodberry 1993) and the GCM (Randall et al. 1991). There are other observations showing diurnal variations with maxima in the afternoon in many regions of the Tropics (e.g., Gray and Jacobson 1977; Albright et al. 1981; Reed and Jaffe 1981; Hartmann and Recker 1986). There are two major reasons for this. First, the influence of continents cannot be totally eliminated in observed datasets. Second, variables other than $\langle P \rangle$ were examined, which could, as shown later, have diurnal cycles with maxima not appearing in the early morning.

The Gray–Jacobson mechanism can work in I05 but not in N05. The differences between the two simulations are not totally negligible, especially the phase delay of 2–3 h in I05, when radiation is interactive. This is also true for other measures of convective activity such as the cloud-scale kinetic energy (not shown). Nevertheless, the similarity of the diurnal variation of $\langle P \rangle$ between I05 and N05 suggests that the Gray–Jacobson mechanism is of secondary importance for explaining the diurnal cycle of oceanic precipitation.

Figure 2 shows the time sequence of the filtered liquid water path (LWP) and ice water path (IWP) deviations (reduced by the mean values in I05) and their sum for I05 and N05. The difference in the time sequence of the LWPs between the two simulations is negligible. The phase difference in the IWP is, however, significant, that is, about 5 h. The sum of the LWP and the IWP shows a 3-h phase difference between I05 and N05, as in $\langle P \rangle$. Therefore, the phase difference in convective activity is related to the lagged response of the upper-tropospheric clouds to the radiative destabilization/stabilization in I05. The positive IWP deviation in I05 lasts until noon. N05 shows a positive IWP deviation during the nighttime and a negative IWP deviation during the daytime.

The time–height cross sections of potential temperature deviations (reduced by the mean value at each level in I05) and relative deviations of water vapor mixing ratio for I05 and N05 are shown in Figs. 3 and 4, respectively. These variables are not filtered. The filtered potential temperature and water vapor mixing ratio are very similar to those shown in Figs. 3 and 4. The deviations in potential temperature are negative throughout the troposphere before 9 h. The maximum positive deviations occur in the late afternoon. In addition, the deviations are larger in the upper troposphere. All of these except for the magnitude of the

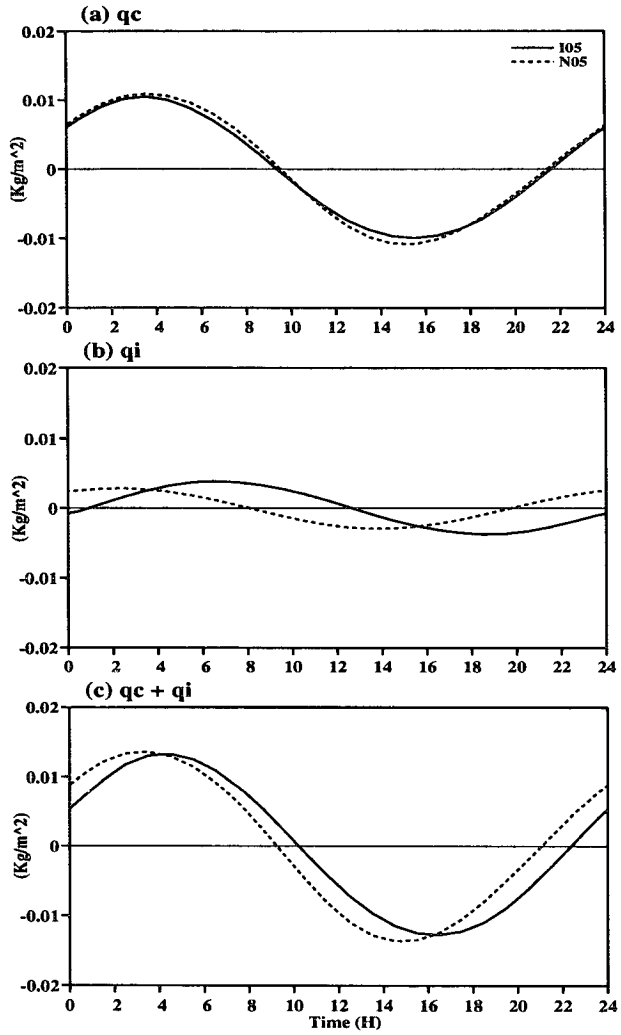

FIG. 2. Time sequence of the ensemble mean of (a) cloud water content, (b) cloud ice content, and (c) their sum for I05 (solid) and N05 (dashed). All variables are subtracted by the means of I05.

deviations in the lower troposphere agree with the GCM simulations by Randall et al. (1991). There are almost no significant differences between the two CEM simulations except for the smaller maximum deviation in the late afternoon in N05, which occurs 2 h later and at a higher level in I05.

There are also differences in the relative (to the mean water vapor at each level of I05) deviations of water vapor mixing ratio between I05 and N05. The upper (lower) troposphere in I05 is much more moist (drier) than that of N05, due to the more extensive upper-tropospheric clouds in I05, as shown in Fig. 5a.

Results shown in Figs. 3 and 4 are similar to the observations (e.g., Albright et al. 1981) except that the maxima and minima occur about 2 h later in the CEM simulations. Albright et al. (1981) observed a late-afternoon $\langle P \rangle$ maximum, however. The similarity in the temperature and water vapor mixing ratio between the simulations and the Albright et al. observations suggests that the observed $\langle P \rangle$ maximum might be associated with the semidiurnal variation, the tides, and/or the influence by the continents. That the observed surface heat flux and surface evaporation rate showed a semidiurnal variation in Albright et al. (1981) also supports this argument. In the CEM, the tides cannot be simulated because its top ($\sim$19 km) is too low.

Figure 6 shows the time–height cross sections of filtered mass flux deviations averaged over the cloudy regions for I05 and N05. The cloudy region is defined where the liquid water plus ice mixing ratio at any CEM grid box at any given level exceeds 1% of the saturation water vapor mixing ratio (Xu and Krueger 1991). The cloud mass flux is defined as the summation of the product of density, vertical velocity, and constant of gravity over the cloudy regions. The common feature between I05 and N05 in Fig. 6 is that the cloud mass flux deviation is positive during the nighttime and negative during the daytime, especially in the lower and middle troposphere. The average subsidence in the clear regions (Fig. 7), which are defined similarly to the cloudy regions except that no cloud water or ice exists at any grid box, shows similar diurnal variations in the two simulations. These results suggest that the Gray–Jacobson mechanism is not the dominant one for explaining the diurnal variation of oceanic precipitation.

There are, however, some significant differences between the two simulations, especially in the upper troposphere. In I05, a positive cloud mass flux deviation appears first in the lower and middle troposphere from the early evening and gradually extends to the upper troposphere. The positive deviation in the upper troposphere can last until late afternoon. In N05, the positive deviation appears during the nighttime and a negative one during the daytime. The average subsidence in the clear regions shows the same difference between the two simulations as the cloud mass flux (Fig. 7c). The maximum difference in the average subsidence between I05 and N05 is approximately 17% of the amplitude of diurnal variation in the average subsidence. This again suggests that the Gray–Jacobson mechanism is of secondary importance. The larger subsidence/cloud mass flux in the upper troposphere of I05 is probably related to the persistence of strong cells in the presence of solar radiation (Starr and Cox 1985), which greatly contributes to the cloud mass flux.

Figure 8 shows the time–height cross section of shortwave, longwave, and total cloud radiative forcings (CRFs) for I05. The CRF is defined as the difference of radiative heating rates between cloudy and clear regions (Cess and Potter 1987; Ramanathan 1987). The cloudy region here is defined differently from that in the calculation of cloud mass flux. In calculating CRFs, an entire CEM column (2 km wide) is included in the cloudy region if the total liquid water (precipi-

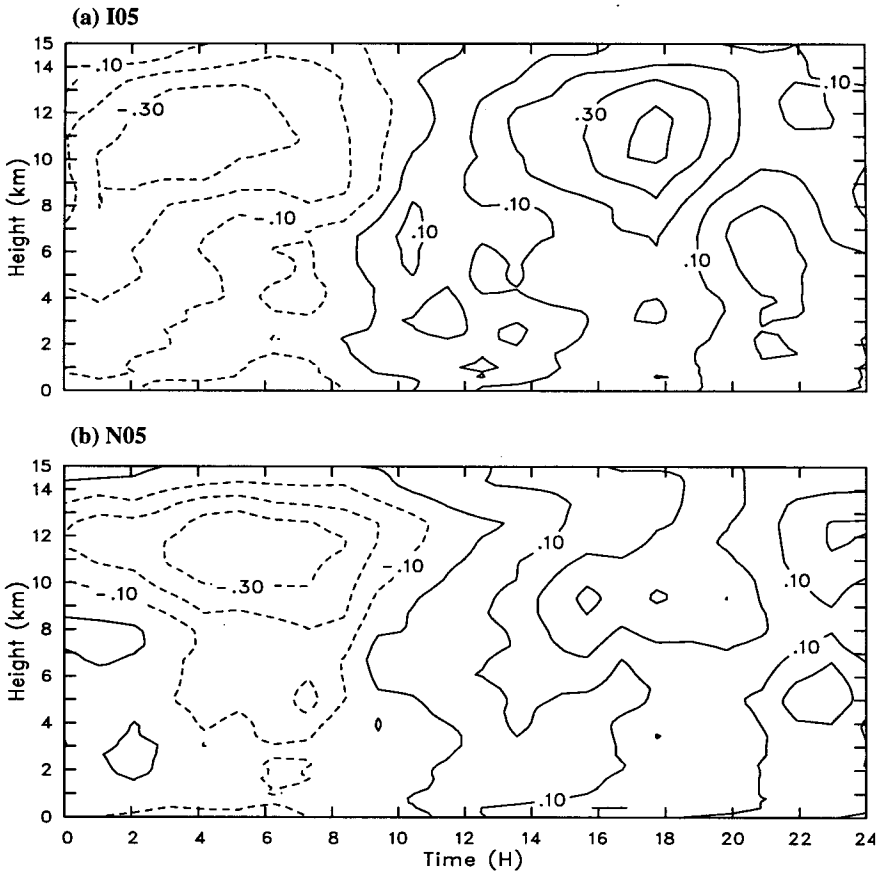

FIG. 3. Time–height cross section of the ensemble mean of potential temperature deviation for (a) I05 and (b) N05. The contour interval is 0.1 K.

tating plus nonprecipitating particles) path exceeds 0.2 kg m^{-2}. A cutoff value is used to avoid including radiatively insignificant cloudy regions. The CRFs shown in Fig. 8 are not filtered. Figure 8a shows that the maximum shortwave CRF appears in the upper troposphere and negative CRF in the lower troposphere, in agreement with GCM simulations by Randall et al. (1991). A difference between the CEM and GCM simulations is the secondary maximum in the middle troposphere. This might be related to a lack of low-level clouds in the GCM. The longwave CRF (Fig. 8b) shows negative values above 11.5 km and positive values below, which is also consistent with the GCM results. It shows little diurnal variation. A small negative CRF appears at 4.5 km due to the low-level clouds. The total CRF (Fig. 8c) also agrees with the GCM results.

The time–height cross section of total latent heating rate deviations (reduced by the mean values at each level in I05) is shown in Fig. 9 for I05 and N05. The diurnal variation is similar between I05 and N05 except for the positive deviation in the upper troposphere during the daytime, which is due to deposition associated with ice clouds in the upper troposphere. Overall, the results shown in Fig. 9 agree with GCM simulations by Randall et al. (1991). Another important point in Figs. 8c and 9a is that there is a 3-h phase difference between the maximum CRF and the minimum latent heating rate. The 3-h difference is much longer than the life cycle of individual clouds but shorter than that of mesoscale cloud clusters. Therefore, the direct radiation–convection interaction mechanism may have to be associated with both individual clouds and their mesoscale circulations.

Figure 10 shows the diurnal variation of the longwave outgoing radiation (OLR) flux for the entire domain and for the cloudy regions of I05. The peak-to-peak variation is approximately 2.5 W m^{-2} for the entire domain and 4.0 W m^{-2} for the cloudy regions. The magnitude is smaller than that observed in the South Pacific convergence zone (e.g., Hartmann and Recker 1986). The minimum OLR for the entire domain appears 3 h later than the maximum $\langle P \rangle$ (Fig. 1b) because the upper-tropospheric clouds continue to develop after deep cumulus convection reaches its maximum intensity. The minimum OLR in the cloudy regions appears just before noon when the upper-tropospheric clouds reach the maximum intensity (Fig. 6a). Therefore, the OLR is probably not a good variable for determining

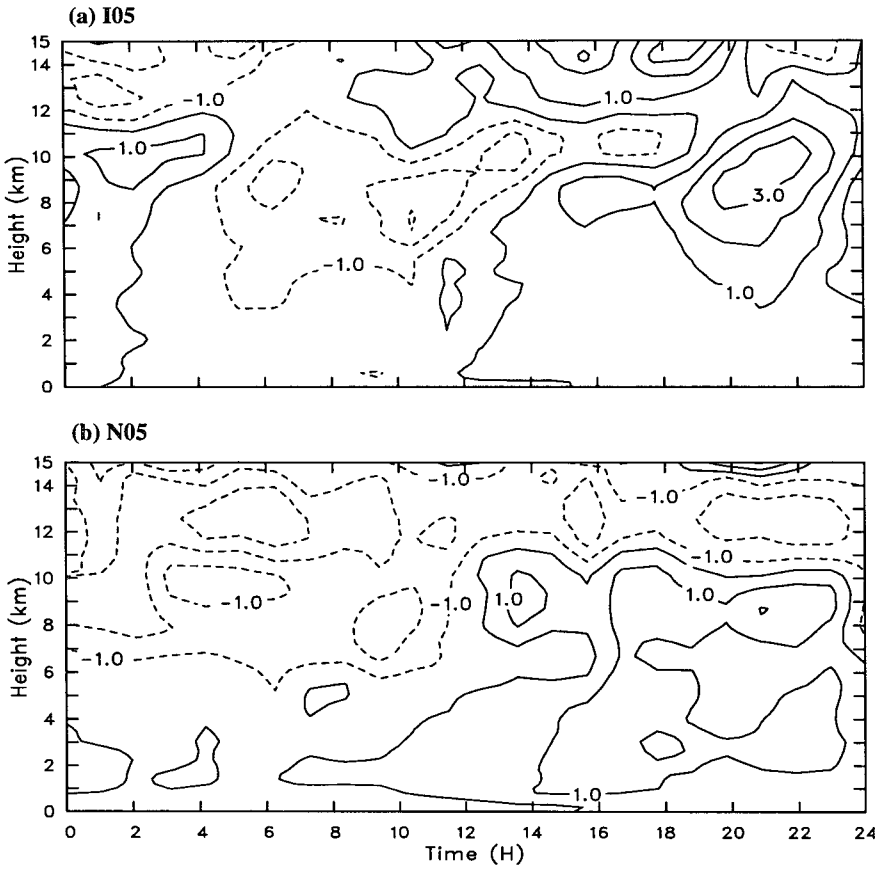

FIG. 4. Time–height cross section of the ensemble mean of the relative deviation of water vapor mixing ratio (with respect to the mean value at each level in I05) for (a) I05 and (b) N05. The contour interval is 1%.

the intensity of deep convection. It is strongly dependent upon the cloud type and height (e.g., Hartmann and Recker 1986).

4. Results: Impact of longwave radiation

Results from simulations I04 and N04, which do not include shortwave radiation, are presented in this section. The impact of longwave radiation on the modulation of cumulus activity by large-scale processes is examined by a comparison of these two simulations.

Xu et al. (1992) examined the modulation of cumulus activity by time-varying large-scale advective processes. A time-independent radiative heating profile (Fig. 1c in Xu et al. 1992) was prescribed in those simulations. The simulations described in this section are similar to those in Xu et al. (1992) except that I04 has an interactive longwave radiative transfer and N04 uses time-varying, domain-averaged radiative heating profiles from I04.

Figure 11 shows the time sequence of the ensemble mean of $\langle P \rangle$, surface evaporation rate $\langle E \rangle$, and $\langle P - E \rangle$, as well as the time variation of the large-scale advective effects $\langle F \rangle$. The ensemble mean in I04 and N04 is defined with respect to the phase of large-scale advective processes, with a period of 27 h. Strong modulation indicates that convective activity, as measured, for example, by $\langle P \rangle$, shown in Fig. 11, is highly correlated with the imposed large-scale advective effects. Figure 11 shows that the modulation in I04 seems to be slightly stronger than that in N04. Otherwise, the difference between I04 and N04 is very small, as far as $\langle P \rangle$ is concerned.

The 15-day averaged $\langle P \rangle$ and $\langle E \rangle$ show no significant differences between I04 and N04 (less than 0.5%). This indicates that the effects of interactive longwave radiation on the intensity of cumulus convection are very weak so long as the total destabilization of the large-scale environment by longwave radiation is identical. Previous studies (e.g., Dudhia 1989; Tao et al. 1993) showed a large increase in surface precipitation rate when a simulation with interactive radiation was compared to that without any radiative cooling; that is, the total destabilization is not identical. The present result should clarify the effects of the horizontal inhomogeneity of radiative heating rate on the

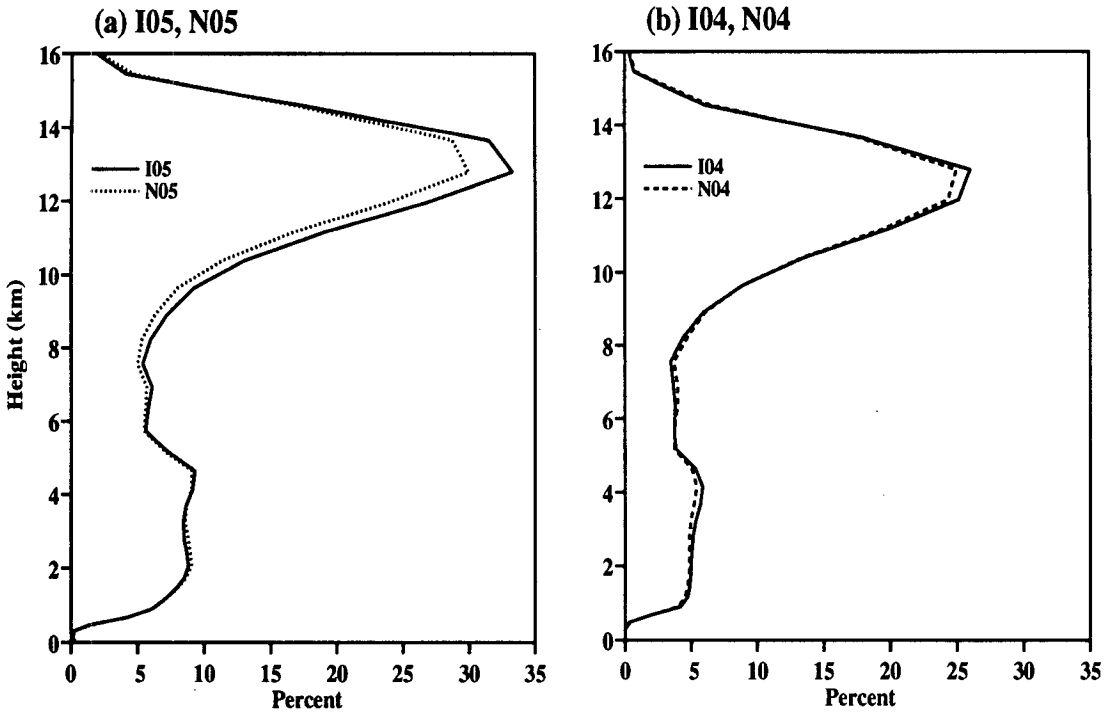

FIG. 5. Vertical profiles of the fractional cloudiness for (a) I05 and N05 and (b) I04 and N04.

intensity of cumulus convection for a given large-scale advective forcing if the integration is not too short. The negligible difference was also simulated with a mesoscale model by Miller and Frank (1993).

Figure 12 shows the time–height cross section of fractional cloud amount for I04 and N04. The cloud amount is the area of cloudy regions as defined in calculating the cloud mass flux in section 3, divided by the total area. The cloud amount is very large in the upper troposphere of both simulations. The largest cloud amount occurs at 13 h of N04. After 14 h, the cloud amount in the upper troposphere of N04 is slightly smaller than that in I04 (looking specifically at the 24% contour in Fig. 12). The larger cloud amount between 14 and 25 h in I04 is related to the greater persistence of anvil clouds due to interactive longwave radiation. Figure 5 shows the 15-day averaged profiles of cloud amount for all simulations. The cloud amount in I04 is slightly larger than in N04 only at ~12 km, while the cloud amount in I05 is larger than in N05 throughout the entire upper troposphere.

Differences in temperature and water vapor mixing ratio between I04 and N04 are also present, although their magnitudes are small. Figure 13 shows time–height cross sections of the potential temperature deviations (reduced by the mean value at each level in I04) for I04 and N04. A common feature between I04 and N04 is the large negative temperature deviation in the upper troposphere between 3 and 10 h. This is due to weak intensity of deep convection (Fig. 11) whose condensational heating cannot compensate the imposed large-scale advective cooling, especially in the upper troposphere. Likewise, positive temperature deviations correspond to strong convective activity (relative to the given large-scale advective process).

The main difference in potential temperature deviations between I04 and N04 is that the atmosphere in I04 is relatively warmer (colder) in the upper (lower) troposphere. This is related to the impact of the greater amount of anvil clouds in I04, which causes more condensational warming (cooling) in the upper (lower) troposphere, in particular after 12 h. Note that the domain-averaged large-scale effects and radiative effects are identical between I04 and N04. The differences in potential temperature and water vapor mixing ratio (not shown) are solely caused by the difference in the intensity of cumulus convection. The atmosphere is also slightly more moist (drier) in I04 than in N04 in the upper (lower) troposphere (not shown). In summary, the aforementioned results suggest that interactive longwave radiation can weakly influence the temperature and moisture structure mainly by changing the intensity of upper-tropospheric clouds.

5. Cloud–radiation interaction mechanisms

Three mechanisms for cloud–radiation interactions are mentioned in the introduction. Which mechanism has the dominant impact on the statistical behavior of cumulus ensembles or is responsible for the differences between interactive and noninteractive simulations?

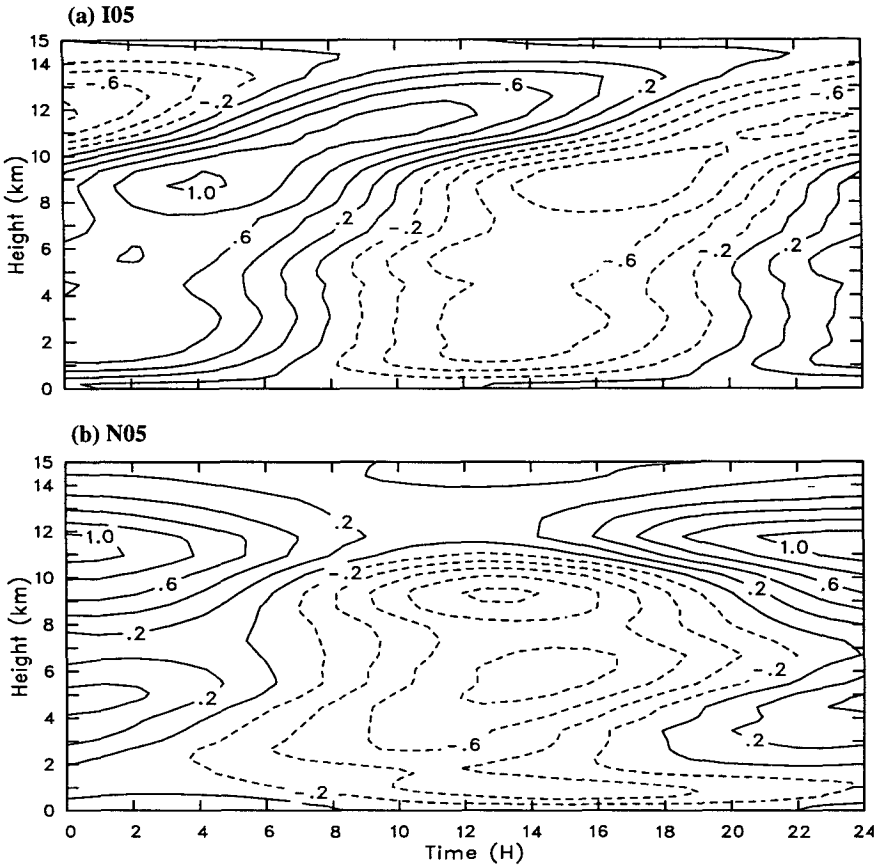

FIG. 6. Time–height cross section of the ensemble mean of mass flux deviation in the cloudy regions for (a) I05 and (b) N05. The contour interval is 0.2 mb h^{-1}.

a. Horizontal differential heating mechanism

The Gray–Jacobson (1977) mechanism has been examined through the comparison of two pairs of simulations discussed in sections 3 and 4. The overall conclusion is that this mechanism does not have a strong impact on the statistical behavior of cumulus ensembles because the differences between the interactive and noninteractive simulations are small. As discussed in the introduction, this mechanism emphasizes the generation of secondary circulations due to horizontal differential heating between cloudy and clear regions; that is, the clear region subsidence would be greater (smaller) in the presence of horizontal differential heating associated with longwave (shortwave) radiation. A comparison of the clear region subsidence between interactive and noninteractive simulations should give some indication of the existence of this mechanism.

Figure 14 shows the same plots as in Fig. 7 except for I04 and N04. A noticeable feature in Figs. 14a,b is that the magnitude of average subsidence is generally greater when $\langle P \rangle$ is higher (Fig. 11) in either simulation, because $\langle P \rangle$ is related mainly to the intensity of deep convection, which induces strong clear region subsidence. Overall, the two simulations do not show any systematic difference related to the presence of horizontal differential heating between cloudy and clear regions (Fig. 14c). This point is also valid for I05 and N05 (see section 3).

Previous studies (e.g., Dudhia 1989; Tao et al. 1991, 1993) showed that the Gray–Jacobson mechanism is important by comparing simulations with either interactive or no longwave radiative transfer. Because the total domain-averaged destabilizing effects are different, the intensity of cumulus convection between such a pair of simulations is expected to be different. The difference cannot be attributed to the cloud–radiation interactions alone. Thus, those studies cannot give a firm conclusion about the importance of the Gray–Jacobson mechanism from their simulations. Miller and Frank (1993) performed a pair of simulations similar to those used in this study except using a mesoscale model with parameterized cumulus convection. Their conclusion is almost identical to that found in this study.

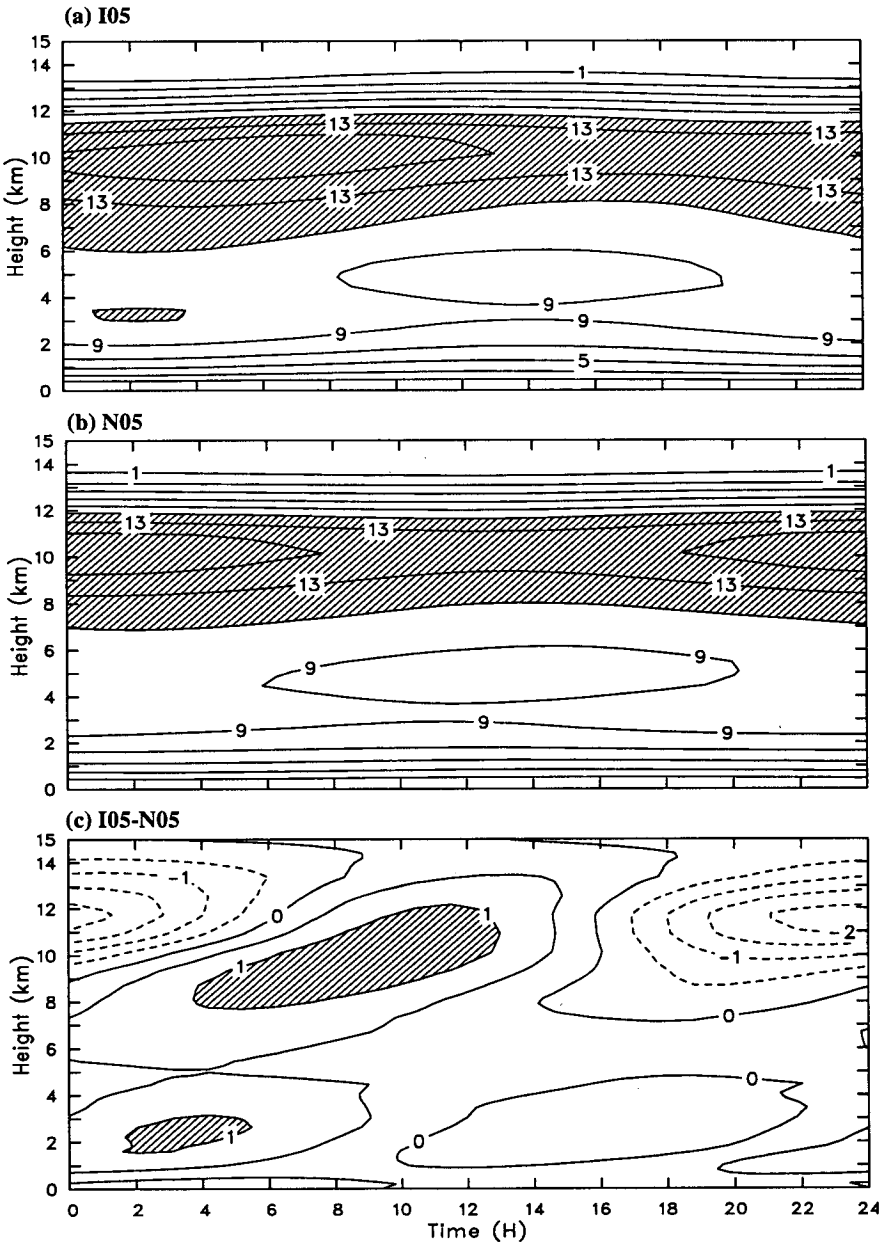

FIG. 7. Time–height cross section of the ensemble mean of average subsidence in the clear regions for (a) I05, (b) N05, and (c) the difference between I05 and N05. The contour interval is 2 mb h^{-1} in (a) and (b) with hatched areas being greater than 11 mb h^{-1}, but 0.5 mb h^{-1} in (c) with hatched areas being greater than 1 mb h^{-1}.

Nevertheless, the circulations in I04 with interactive longwave radiation, as measured, for example, by the cloud-scale kinetic energy [see Xu et al. (1992) for the definition of CKE] are slightly stronger than in the non-interactive simulation N04. The difference is 1.2% for the horizontal CKE and 3.0% for the vertical CKE, which cannot be proved to be significant with a t test. The difference might also be caused by other mechanisms discussed below.

b. In-cloud radiative heating/destabilization mechanism

Lilly (1988) proposed a mechanism based on in-cloud radiative heating and radiative destabilization for generating buoyant turbulence in anvil clouds. He stated:

> The dynamic structure of outflow cirrus is here idealized as a two-stage process. The initial outflow from a

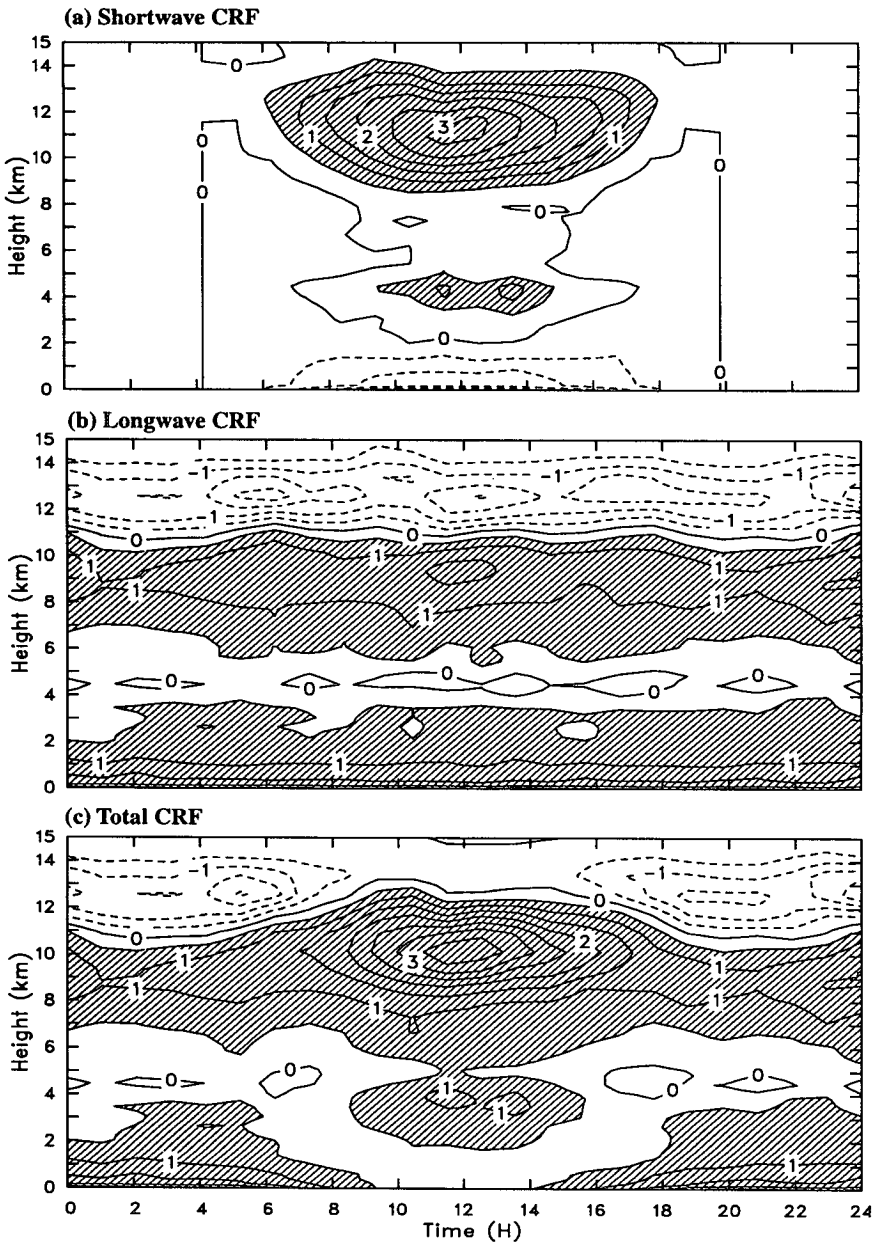

FIG. 8. Time–height cross section of the ensemble mean of (a) shortwave cloud radiative forcing (CRF), (b) longwave CRF, and (c) their sum for I05. The contour interval is 0.5 K d^{-1}. Contours over 0.5 K d^{-1} are hatched.

thunderstorm is an intrusion of air of nearly uniform buoyancy, containing three-dimensional, nearly isotropic, turbulence, into an otherwise stably stratified environment . . . The second stage of outflow plume development is the radiative destabilization of the outflow layer, leading to convectively generated turbulence and growth by entrainment at the top and bottom . . . In the case of strong net radiative heating, the mixed layer model predicts an encroachment condition, in which the upper boundary attains nearly the same temperature as the environment and grows into it rapidly.

Lilly's mechanism has not previously been examined with data obtained from explicit simulation of cumulus ensembles. The first thing is to look at the mean profiles of turbulent kinetic energy (TKE) and the radiative heating rates in the upper troposphere. Figure 15a shows the parameterized TKE, predicted by a third-moment turbulence closure [see Krueger (1988) for details], averaged over the entire domain and the entire simulation period for I04 and N04. The TKE in I04 is indeed greater than that in N04 between 9 and 13 km,

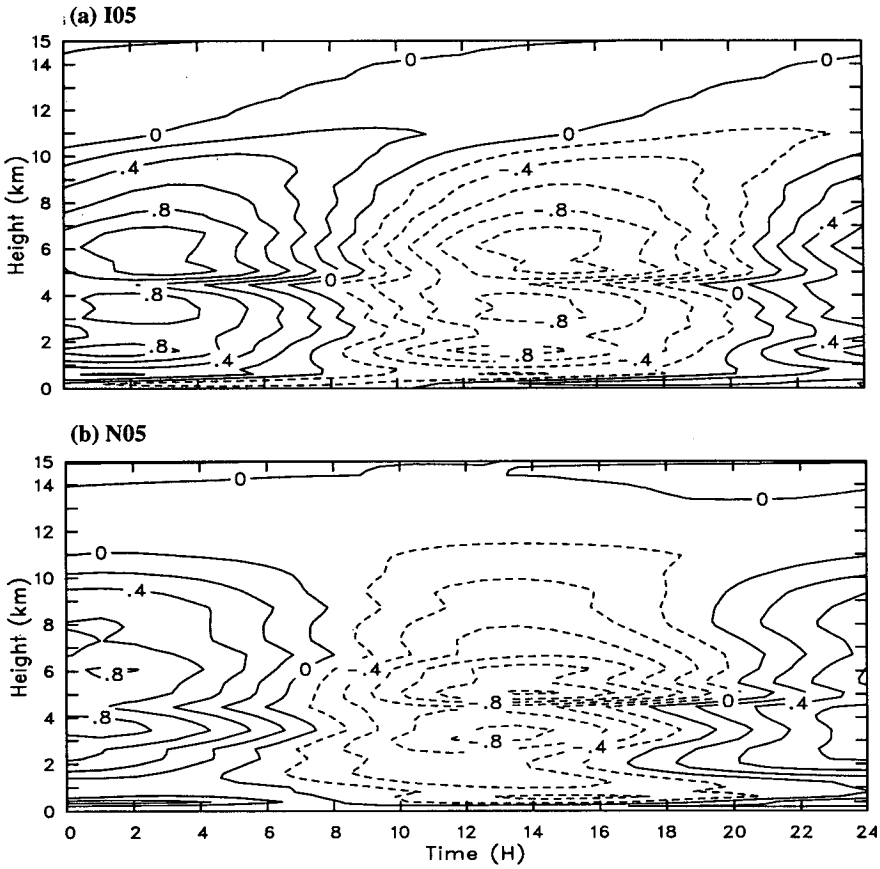

FIG. 9. Time–height cross section of the ensemble mean of the deviations of total latent heating rate for (a) I05 and (b) N05. The contour interval is 0.2 K d^{-1}.

with the greatest increase of 14% at 12 km. This increase is not solely due to the increase of the anvil areas (Figs. 12 and 5b) because the TKE per unit area also shows a similar increase (not shown). Thus, the TKE does increase in the upper troposphere due to the presence of interactive longwave radiation.

Figure 15b shows the radiative heating rates as averaged over the entire domain and over clear regions and cloudy regions of I04, for the entire simulation period. The regions are defined for CEM columns as in the calculation of CRF discussed in section 3. On average, the cloudy regions are cooled by longwave radiation more than in the clear regions above 11 km and warmed more below 11 km. The radiative destabilization of cloud layers is clearly present between 9 and 13 km (Fig. 15b); that is, more cooling at 13 km than at 9 km. This is the layer where TKE increases most (Fig. 15a). For the noninteractive simulation N04 no radiative destabilization is present in the upper troposphere (solid curve in Fig. 15b). Thus, Lilly's mechanism cannot work in N04.

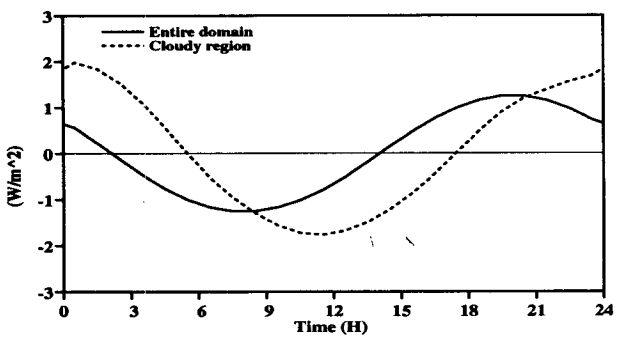

FIG. 10. Time sequence of the outgoing longwave radiation flux deviations for the entire domain and for the cloudy regions of I05.

The mean vertical profiles give some indication of the existence of Lilly's mechanism. They cannot, however, tell how each cloud is affected by this mechanism. Some statistical results are useful in this regard using instantaneous output data sampled every 5 min. First, some definitions used in the calculation are given here. The cloud top is identified where the liquid water (cloud water, cloud ice, and snow) path integrated from the model top reaches 0.005 kg m^{-2}. The cloud base is identified similarly except that the integration of liquid water path starts from the bottom of the model. The

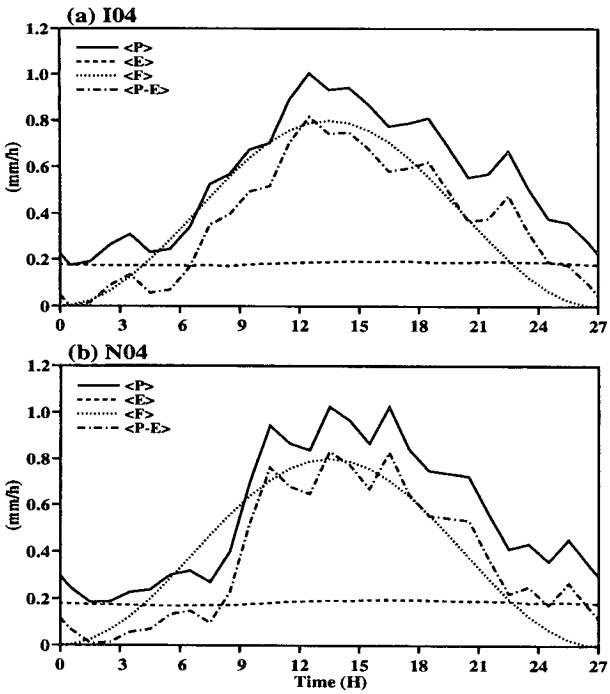

FIG. 11. Time sequence of the ensemble mean of surface precipitation rate, surface evaporation rate, and their difference, as well as the prescribed large-scale effect $\langle F \rangle$ for (a) I04 and (b) N04. The abscissa is the phase of the imposed large-scale advective processes.

snow mixing ratio is also included because it is important to radiative transfer (see Part I). The integration is performed on a CEM grid (2 km wide) column. If several adjacent columns are identified with the same cloud top and base heights, an average is taken to define a cloud. Otherwise, a single CEM column corresponds to a cloud for the statistical analysis.

Three variables are used in the following calculation of correlation coefficients—that is, the radiative destabilization rate, the TKE of cloud layer, and the vertical cloud-scale kinetic energy (VCKE) of the cloud layer. The cloud layer is defined from the cloud base to cloud top. The radiative destabilization rate is defined as the difference of radiative cooling rates between cloud top and cloud base; that is,

$$\Delta Q_R = -[Q_R(\text{top}) - Q_R(\text{base})],$$

where Q_R is the radiative heating rate. So, the time-change rate of lapse rate for the cloud layer is $\Delta Q_R/(z_t - z_b)$, where z_t and z_b are the cloud top and base heights, respectively. The TKE (K_t) and VCKE (K_c) of the cloud layer are defined, respectively, as

$$K_t = \int_{z_b}^{z_t} (u''^2 + v''^2 + w''^2)\rho dz,$$

$$K_c = \int_{z_b}^{z_t} w'^2 \rho dz,$$

where u'', v'', and w'' are the velocity components of turbulent motion, w' is the cloud-scale vertical velocity, and ρ is the air density.

Because Lilly's mechanism applies to cirrus outflows in the upper troposphere, clouds having their bases below 5.5 km are *excluded* in the calculation; that is, all deep convective clouds are excluded even though their tops reach the upper troposphere. Table 2 shows the correlation coefficients between ΔQ_R and K_t for I04. The correlation coefficient for all clouds with various base and top heights is 0.35. This is not very high. The correlation coefficients are then recalculated from data stratified according to the cloud-base height (the eighth column in Table 2). The correlation coefficient is reasonably high for clouds having their bases between 7 and 11 km.

The data are then further stratified according to the thickness of the clouds for a given cloud-base height (columns 2–7 in Table 2). The most interesting feature is that the high correlation coefficients are associated with thick clouds for a given cloud-base height. This result is intriguing and thus needs an explanation.

To understand the results in Table 2, Table 3 shows some statistics specifically for clouds having their bases between 7 and 8 km. Here $R0$ is the correlation coefficient between ΔQ_R and K_t as shown in Table 2. The mean liquid water (cloud water, cloud ice, and snow) mixing ratio $\overline{q_l}$ and the mean K_t, $\overline{\text{TKE}}$, for all clouds with their bases between 7 and 8 km and with a specific thickness are shown; $R1$ is the correlation coefficient between q_l and K_t; $R2$ ($R3$) is the correlation coefficient between ΔQ_R and K_t; for those clouds with q_l greater (smaller) than $\overline{q_l}$.

Table 3 shows that $\overline{q_l}$ increases significantly as clouds become *thicker*. $\overline{\text{TKE}}$ does not, however, increase much for thin clouds (<150 mb), and the correlation between q_l and TKE is very low for these clouds. This result suggests that TKE is not necessarily increased as these clouds become optically thicker. For these clouds, TKE is better correlated with ΔQ_R if they are optically thicker because $R2$ is always much greater than $R3$. For thick clouds (>200 mb), this is not true. There are three reasons for it. First, $\overline{q_l}$ of these clouds is much larger than that of thin clouds such that the division becomes less meaningful in calculating R2 and R3. Second, different vertical distributions of q_l in thick clouds can greatly change ΔQ_R. Third, snow mixing ratio can greatly contribute to q_l of thick clouds such that ΔQ_R becomes smaller due to small radiative effects of snow particles (see Part I).

The results in Tables 2 and 3 suggest that TKE is increased in response to the increase of radiative destabilization effects. A possible scenario might be as follows. Once a thin cloud is generated, the radiative destabilization occurs. The change of temperature stratification due to radiative destabilization cannot occur instantaneously and the TKE may not increase imme-

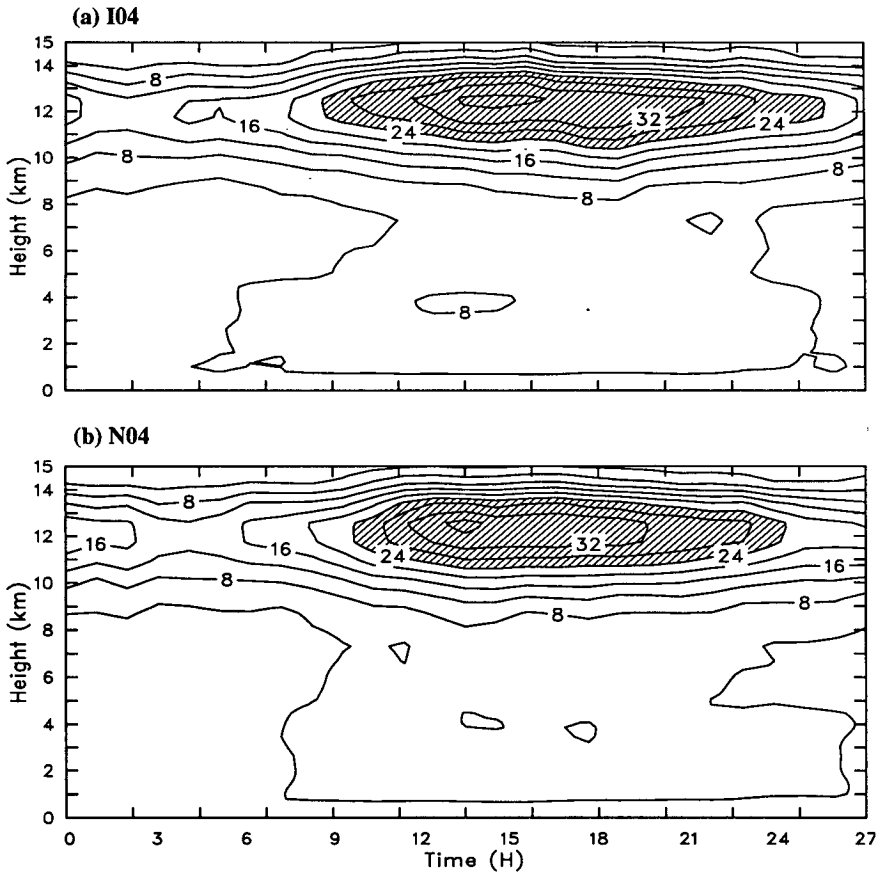

FIG. 12. Time–height cross section of the ensemble mean of the fractional cloud amounts for (a) I04 and (b) N04. The contour interval is 4%. Contours over 24% are hatched.

diately, especially for optically thin clouds. For a thick cloud, the change of temperature stratification has occurred due to continuous radiative destabilization and thus the TKE in the cloud layer increases in response to the radiative destabilization. Therefore, a high $R0$ is expected for thick clouds.

c. *Vertically continuous destabilization mechanism*

The mean vertical profile of radiative heating rates averaged over cloudy regions (e.g., dashed curve in Fig. 15b) has been previously used for arguing the negligible importance of the vertically continuous destabilization mechanism as first proposed by Webster and Stephens (1980; see Tao et al. 1991, 1993; Churchill and Houze 1991; Miller and Frank 1993; Sui et al. 1994). This is, however, not appropriate because the magnitude of cloud-top cooling and cloud-base warming is greatly smoothed out due to the variation of cloud-base and cloud-top heights. Therefore, a more appropriate argument should be based on the statistics of clouds with same base and top heights.

First, Fig. 15c shows the mean cloud-top radiative heating rate and mean cloud-base radiative heating rate (solid lines), as well as their extreme values (dotted lines) for I04. The mean cloud-top cooling rate is between 11 and 18 K d^{-1}, while the mean cloud-base heating rate is between 3 and 5 K d^{-1}. The mean cloud-top cooling rate is relatively large in the lower troposphere. Thus, for a fixed thickness of clouds the destabilizing effects are greater for clouds having their tops below 6 km. This suggests that the destabilizing effects are, on average, slightly more significant for lower-tropospheric clouds. This may explain a rapid enhancement of convection between 6 and 9 h in I04 than in N04 (Figs. 12 and 14).

The profile of extreme cloud-top heating rate shows a minimum at ~8 km. This profile bears little similarity to the mean cloud-top heating profile because the cloud with the maximum liquid water content is usually associated with the extreme value. The profile is similar to that shown by Dudhia (1989) for an idealized calculation for varying cloud-top heights and varying cloud-base heights, except with greater magnitudes. One interesting feature appearing in the extreme cloud-

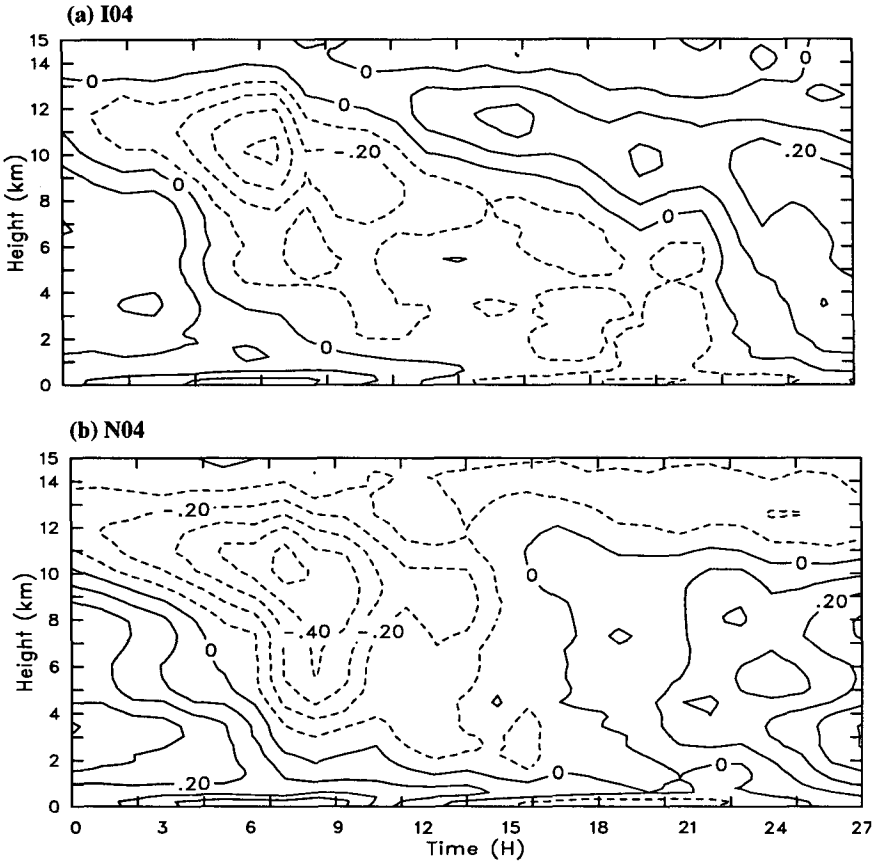

FIG. 13. Same as Fig. 3 except for I04 and N04. The contour interval is 0.1 K.

base heating profile is that the extreme value is far greater than the mean value in the upper troposphere. (Note that strong cloud-base warming requires clear, dry air below the cloud base and an optically thick cloud above.) This result suggests that the destabilizing effects are significant for some high, upper-tropospheric clouds. The large correlation between ΔQ_R and the LWP in the upper troposphere (e.g., 0.87 for cloud base at 9.28 km, 0.50 for cloud base at 6 km) is one of the indicators.

Second, Fig. 15d shows the mean value of the radiative destabilization rate ΔQ_R as a function of cloud thickness. A striking result in Fig. 15d is that the destabilization rate is the greatest for the thin clouds (thinner than 200 mb). This is consistent with a theoretical calculation for anvil clouds by Ackerman et al. (1988). For deep cumulus clouds with large LWPs (dashed curve in Fig. 15d), the radiative destabilization rate is also very large. Because the very large thickness of this type of clouds, the effects of radiative destabilization on the temperature lapse rate are small. Therefore, Fig. 15d indicates that the radiative destabilization effect has the greatest influence on the thin clouds, especially for clouds having their tops in the lower troposphere or above 8 km (Fig. 15c; Table 2). The destabilizing effects of radiation are most effective for *thin* clouds.

The radiative destabilization rate ΔQ_R is not highly correlated with cloud-scale kinetic energy (CKE), as shown in Table 4, which is similar to Table 2 except for correlation coefficients between K_c and ΔQ_R. The correlation coefficients in Table 4 are generally smaller than those in Table 2. They are, however, greater for thicker clouds (>150 mb). This implies that the radiative destabilization takes longer to generate cloud-scale vertical motions than to generate turbulence-scale motions. That is, the destabilization of cloudy layers has to be continuous to be effective.

In summary, the mechanism of continuous destabilization by radiation is more important than has been argued by previous studies (Dudhia 1989; Tao et al. 1991, 1993; Churchill and Houze 1991; Miller and Frank 1993) except Chen and Cotton (1988). The mechanism can be envisioned as a two-step process: first the turbulent motion is enhanced more or less instantaneously, and then the cloud-scale motion is enhanced more gradually. The longevity of upper-tropospheric clouds in

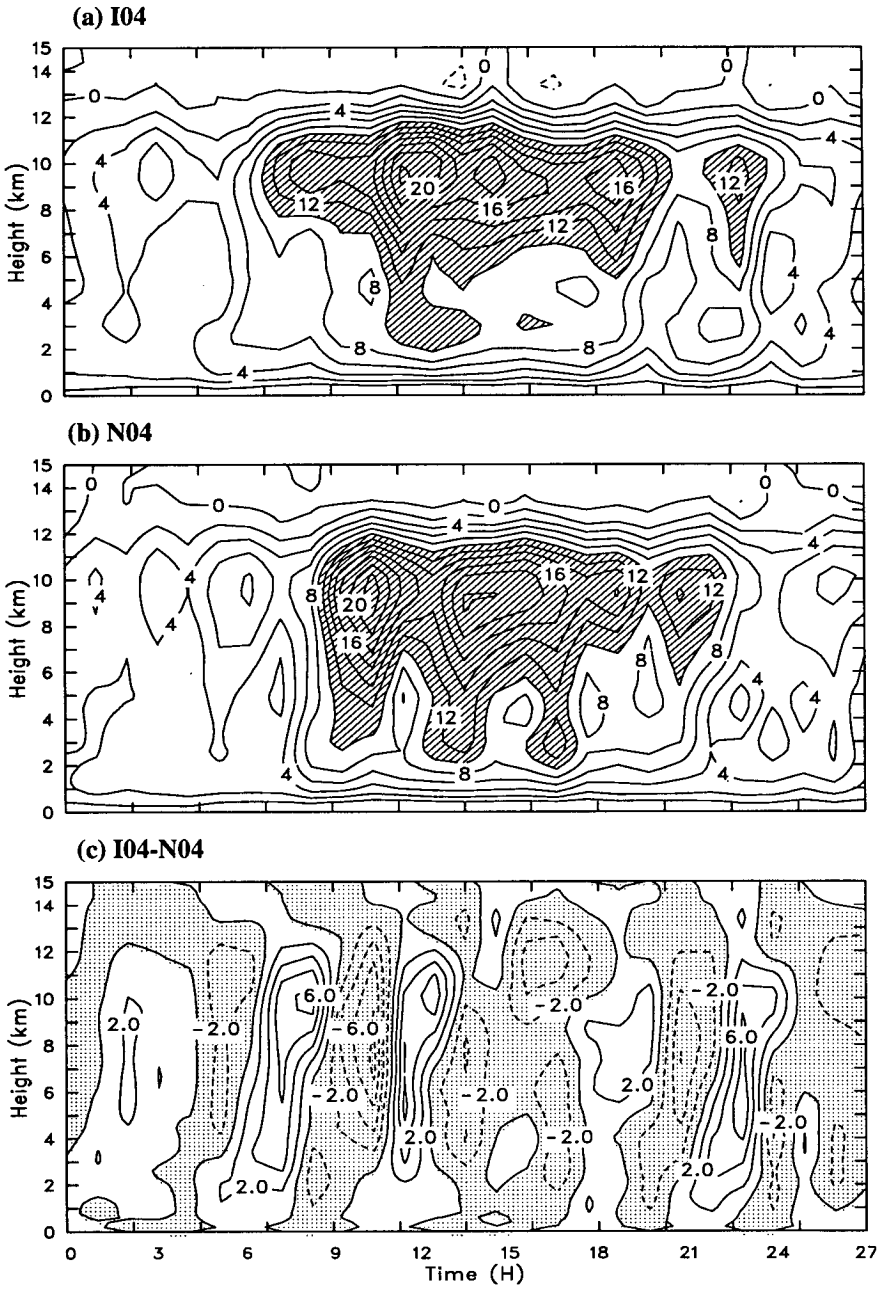

FIG. 14. Same as Fig. 7 except for I04 and N04. The contour interval is 2 mb h^{-1}. Contours over 10 mb h^{-1} in (a) and (b) are hatched. Contours less than 0 mb h^{-1} are dotted in (c).

both interactive simulations (I04 and I05) can be explained by this mechanism. The greater persistence of upper-tropospheric clouds during the daytime in I05 can be related to in-cloud heating, which increases the radiative destabilization of thin upper-tropospheric clouds. Starr and Cox (1985) argued that more strong individual cells in the cirrus outflow can be generated during the daytime. The statistical results above can only be qualitatively discussed because of the sensitivity of radiative heating rate to the vertical resolution and many other uncertainties of the model. Overall conclusions should not be greatly changed, however.

6. Summary and discussion

Explicit simulations of cumulus ensembles have been performed to examine the impact of cloud–radi-

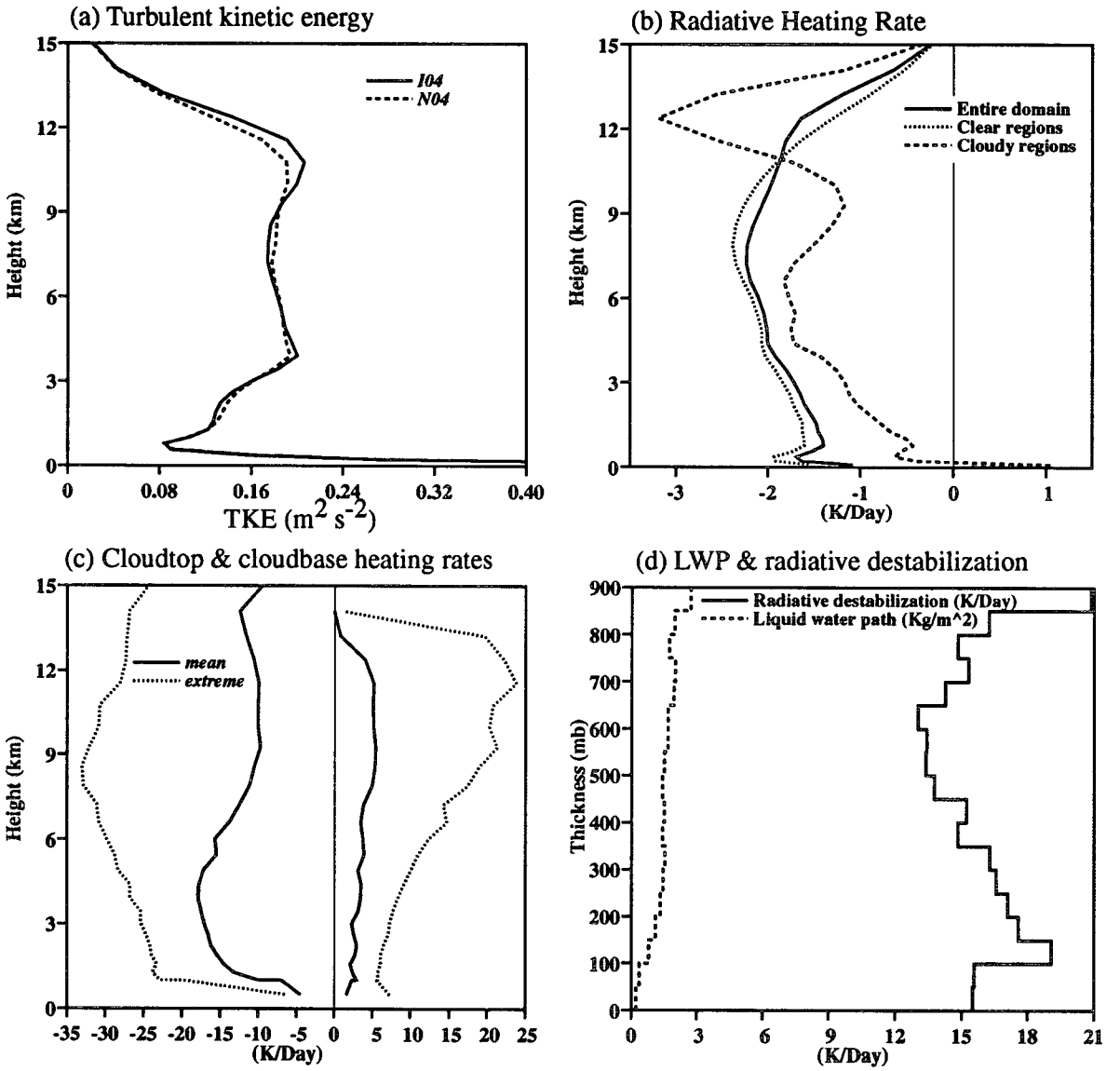

FIG. 15. Vertical profiles of (a) turbulent kinetic energy for both I04 and N04, (b) radiative heating rate over the entire domain, clear regions, and cloudy regions, (c) cloud-base and cloud-top radiative heating rates, and (d) liquid water path and radiative destabilization rate as a function of cloud thickness for simulation I04 only.

ation interactions on the macroscopic behavior of cumulus convection. A unique aspect of this study is the comparison of the results between a set of two simulations that have the same domain-averaged radiative heating rates, but without the horizontal inhomogeneity of radiative heating (noninteractive) in one of the simulations. The impact of both longwave radiation and diurnally varying solar radiation has been examined. The mechanisms for cloud–radiation interactions and for diurnal variations of oceanic precipitation have been explored in detail.

The effects of diurnally varying solar radiation on oceanic precipitation have been investigated, with an emphasis on two mechanisms, that is, the radiation–dynamics–convection interaction (Gray and Jacobson 1977) and the direct radiation–convection interaction. The former emphasizes the diurnal variation in the large-scale/mesoscale vertical motion, and the latter emphasizes daytime stabilization by solar absorption in the upper portion of the cloud masses. The simulations with interactive or noninteractive radiation produce almost identical diurnal variations of

TABLE 2. Correlation coefficients between turbulent kinetic energy and radiative destabilization rate for I04. Clouds are classified according to their base heights (row) and thicknesses (column). "All" combines all clouds with different base heights (bottom row) or thicknesses (eighth column).

	Thickness (mb)						
Cloud-base height (km)	<50	50–100	100–150	150–200	200–250	>250	All
>12	−0.1	0.53					−0.09
11–12	0.03	0.35					0.11
10–11	0.21	0.39	0.54				0.40
9–10	0.17	0.33	0.57	0.48			0.48
8–9	0.30	0.44	0.45	0.64	0.56		0.54
7–8	0.15	0.29	0.38	0.51	0.52	0.52	0.43
5.5–7	0.02	0.11	0.37	0.36	0.37	0.34	0.30
All	0.10	0.28	0.38	0.49	0.45	0.35	0.35

precipitation, and these are consistent with observations. This suggests that the Gray–Jacobson mechanism is of secondary importance for explaining the diurnal variation of oceanic precipitation. Obviously, the diurnal variation of solar absorption in the upper troposphere is responsible for the diurnal cycle of precipitation whether its effect is horizontally homogeneous or not. With interactive radiation, however, more ice clouds are generated in the upper troposphere by the continuous destabilization of cloudy layers due to infrared radiation during the nighttime. These clouds slowly respond to radiative destabilization in the nighttime and can survive in spite of the stabilizing effects of solar absorption during the daytime, presumably due to the radiative destabilization caused by in-cloud heating so that the thin upper-tropospheric clouds can be maintained. The thermodynamic structure of the atmosphere is also affected by the presence of these clouds.

The CEM simulations have also been used to check some important aspects of GCM simulations by Randall et al. (1991). The CEM simulations of the diurnal cycle of oceanic precipitation produce results very similar to those of the CSU GCM simulations. This suggests that the parameterization of convection in the CSU GCM is reasonably successful.

The modulation of cumulus activity by the time-varying large-scale advective effects is slightly stronger in the presence of interactive longwave radiation. With interactive radiation, anvil clouds are more active and last longer. These clouds can weakly influence the thermodynamic structure of the atmosphere.

A two-step process can be described for the radiative destabilization mechanism. The radiative destabilization enhances the turbulent-scale motions more or less instantaneously. It then takes a longer time to enhance the cloud-scale motions. The destabilization is more effective for thin clouds, which generally possess the greatest amount of radiative destabilization. This study reveals that continuous destabilization acts on the cloud-scale motions through Lilly's (1988) mechanism of radiative destabilization in the cloudy upper troposphere. On the other hand, the Gray–Jacobson (1977) mechanism of horizontal differential heating between cloudy and clear regions, generating secondary circulations, is not supported by the results of this study. A simple explanation for this can be based on the differences between the horizontal and vertical scales of convective circulations, and the magnitudes of the differential heating. The effects of vertical differential heating are simply much stronger than those of horizontal differential heating.

Further studies are under way to understand the factors determining the amplitude of the diurnal and semidiurnal cycles and the occurrence of maximum and minimum convection under different large-scale conditions. Preliminary results show that the amplitude and phase of the diurnal cycle are related to the organization of convective systems and the magnitude of the large-scale forcing.

TABLE 3. Statistics for clouds with bases between 7 and 8 km as classified according to their thicknesses: R_0 is the correlation coefficient between turbulent kinetic energy (TKE) and radiative destabilization rate, $\overline{q_l}$ is the averaged liquid water mixing ratio, $\overline{\text{TKE}}$ is the averaged TKE, R_1 is the correlation coefficient between ql and TKE, and R_2 (R_3) is the same as $R0$ except for those clouds with ql greater (smaller) than $\overline{q_l}$.

	Variables					
Thickness (mb)	R_0	$\overline{q_l}$ (g kg^{-1})	$\overline{\text{TKE}}$ (m^2 s^{-2})	R_1	R_2	R_3
<50	0.15	0.0046	0.0117	0.06	0.21	0.08
50–100	0.29	0.0067	0.0108	0.20	0.32	0.07
100–150	0.38	0.0085	0.0120	0.37	0.43	0.12
150–200	0.51	0.0120	0.0179	0.49	0.54	0.08
200–250	0.52	0.0225	0.0460	0.55	0.37	0.26
>250	0.52	0.0378	0.1228	0.43	0.40	0.57

TABLE 4. Same as Table 2 except for the correlation coefficients between vertical cloud-scale kinetic energy and radiative destabilization rate.

Cloud-base height (km)	Thickness (mb)						
	<50	50–100	100–150	150–200	200–250	>250	All
>12	0.00	0.08					0.00
11–12	0.06	−0.01					−0.03
10–11	0.03	0.02	0.10				0.05
9–10	−0.10	0.03	0.11	0.22			0.14
8–9	−0.07	−0.02	0.06	0.25	0.47		0.30
7–8	0.05	0.03	0.06	0.23	0.40	0.43	0.30
5.5–7	−0.01	−0.02	0.10	0.09	0.20	0.31	0.25
All	0.00	0.02	0.05	0.21	0.33	0.32	0.26

Acknowledgments. Discussions with Professors Graeme Stephens, Harshvardhan, and William Gray and Dr. Takmeng Wong are appreciated. The authors thank Prof. Dean Churchill and two anonymous reviewers for their valuable comments. This study was supported by the U.S. Department of Energy's Atmospheric Radiation Measurement program under Grant DE-FG02-92ER61363.

REFERENCES

Ackerman, T. P., K.-N. Liou, F. P. J. Valero, and L. Pfister, 1988: Heating rates in the tropical anvils. *J. Atmos. Sci.*, **45,** 1606–1623.

Albright, M. D., D. R. Mock, E. E. Recker, and R. J. Reed, 1981: A diagnostic study of the diurnal rainfall variation in the GATE B-scale area. *J. Atmos. Sci.*, **38,** 1429–1445.

Cess, R. D., and G. L. Potter, 1987: Exploratory studies of cloud radiative forcing with a general circulation model. *Tellus,* **39A,** 460–473.

Chen, S., and W. R. Cotton, 1988: The sensitivity of a simulated extratropical mesoscale convective system to longwave radiation and ice-phase microphysics. *J. Atmos. Sci.*, **45,** 3897–3910.

Churchill, D. D., and R. A. Houze Jr., 1991: Effects of radiation and turbulence on the diabatic heating and water budget of the stratiform region of a tropical cloud cluster. *J. Atmos. Sci.*, **48,** 903–922.

Dudhia, J., 1989: Numerical study of convection observed during the winter monsoon experiment using a mesoscale two-dimensional model. *J. Atmos. Sci.*, **46,** 3077–3107.

Gray, W. M., and R. W. Jacobson Jr., 1977: Diurnal variation of deep cumulus convection. *Mon. Wea. Rev.*, **105,** 1171–1188.

Hartmann, D. L., and E. E. Recker, 1986: Diurnal variation of outgoing longwave radiation in the tropics. *J. Climate Appl. Meteor.*, **25,** 800–812.

Hendon, H. H., and K. Woodberry, 1993: The diurnal cycle of tropical convection. *J. Geophys. Res.*, **98,** 16 623–16 637.

Krueger, S. K., 1988: Numerical simulation of tropical cumulus clouds and their interaction with the subcloud layer. *J. Atmos. Sci.*, **45,** 2221–2250.

Lilly, D. K., 1988: Cirrus outflow dynamics. *J. Atmos. Sci.*, **45,** 1594–1605.

Miller, R. A., and W. M. Frank, 1993: Radiative forcing of simulated tropical cloud clusters. *Mon. Wea. Rev.*, **121,** 482–498.

Murakami, M., 1979: Large-scale aspects of deep convective activity over the GATE area. *Mon. Wea. Rev.*, **107,** 994–1013.

Ramanathan, V., 1987: The role of earth radiation budget studies in climate and general circulation research. *J. Geophys. Res.*, **92,** 4075–4095.

Randall, D. A., Harshvardhan, and D. A. Dazlich, 1991: Diurnal variability of the hydrological cycle in a GCM. *J. Atmos. Sci.*, **48,** 40–62.

Reed, R. J., and K. D. Jaffe, 1981: Diurnal variation of summer convection over West Africa and the tropical eastern Atlantic during 1974 and 1978. *Mon. Wea. Rev.*, **109,** 2527–2534.

Starr, D. O'C., and S. K. Cox, 1985: Cirrus clouds. Part II: Numerical experiments on the formation and maintenance of cirrus. *J. Atmos. Sci.*, **42,** 2682–2694.

Sui, C.-H., K.-M. Lau, W.-K. Tao, and J. Simpson, 1994: The tropical water and energy cycle in a cumulus ensemble model. Part I: Equilibrium climate. *J. Atmos. Sci.*, **51,** 711–728.

Tao, W.-K., J. Simpson, and S.-T. Soong, 1991: Numerical simulation of a subtropical squall line over the Taiwan Strait. *Mon. Wea. Rev.*, **119,** 2699–2723.

——, ——, C.-H. Sui, B. Ferrier, S. Lang, J. Scala, M.-D. Chou, and K. Pickering, 1993: Heating, moisture and water budgets of tropical and midlatitude squall lines: Comparisons and sensitivity to longwave radiation. *J. Atmos. Sci.*, **50,** 673–690.

Webster, P. J., and G. L. Stephens, 1980: Tropical upper troposphere extended clouds: Inferences from winter MONEX. *J. Atmos. Sci.*, **37,** 1521–1541.

Xu, K.-M., and S. K. Krueger, 1991: Evaluation of cloudiness parameterization using a cumulus ensemble model. *Mon. Wea. Rev.*, **119,** 342–367.

——, and D. A. Randall, 1995: Impact of interactive radiative transfer on the macroscopic behavior of cumulus ensembles. Part I: Radiation parameterization and sensitivity test. *J. Atmos. Sci.*, **52,** 785–799.

——, A. Arakawa, and S. K. Krueger, 1992: The macroscopic behavior of cumulus ensembles simulated by a cumulus ensemble model. *J. Atmos. Sci.*, **49,** 2404–2420.